

Article

# Experimental Investigation of Perceptual Characteristics of Functional Cemented Backfilling Materials in Coal Mines

Hengfeng Liu <sup>1</sup>, Jixiong Zhang <sup>1,\*</sup>, Weiqing Zhang <sup>1</sup>, Feng Gao <sup>2</sup>, Hao Yan <sup>1</sup> and Tailong An <sup>3</sup>

<sup>1</sup> State Key Laboratory of Coal Resources and Safe Mining, China University of Mining & Technology, Xuzhou 221116, China; cumtlhfeng@163.com (H.L.); weiqingzhang2010@gmail.com (W.Z.); cumtyhao@163.com (H.Y.)

<sup>2</sup> State Key Laboratory for Geomechanics and Deep Underground Engineering, China University of Mining & Technology, Xuzhou 221116, China; fgao@cumt.edu.cn

<sup>3</sup> Professional and Technical Service Center of Inner Mongolia Coal Industry, Hohhot 010020, China; anhongcumt@126.com

\* Correspondence: zjxiong@cumt.edu.cn; Tel.: +86-139-1200-5505

Received: 27 November 2018; Accepted: 3 January 2019; Published: 17 January 2019



**Abstract:** For investigating perceptual stress characteristics of Functional Cemented Backfilling Materials (FCBM) in coal mines, we prepared functional specimens based on Cemented Backfilling Materials (CBM) with the perceptual stress ability, and clarified their conductive mechanism, perceptual mechanism, and possible engineering applications. Using mechanical tests and the network parallel dynamic method, the mechanical and electrical properties of the prepared materials and the perceptual characteristics under mechanical–electric coupling conditions were analyzed in depth. The test results demonstrate that the deformation of FCBM obeys standard stress–strain rules, while the conductive phase addition can deteriorate their mechanical properties and simultaneously enhance the electrical conductivity of materials. Through fitting, the percolation threshold was determined to be 9.85%. Before the failure, the spatial distribution of the apparent resistivity in the materials was shown to follow the X-shaped radial pattern; after the failure, the material apparent resistivity obeys different distribution rules at various stages. The apparent resistivity of FCBM is negatively correlated with the strain value at the elastic and plastic stages and positively correlated with it at the failure stage. When the graphite content exceeds the percolation threshold, the materials exhibit a favorable perceptual functionality at the elastic stage.

**Keywords:** functional backfilling; cementing backfilling; network parallel electrical method; mechanical-electrical response

## 1. Introduction

The physical and mechanical properties of Cemented Backfilling Materials (CBM) are critical for filling performance control, and a robust monitoring technique is required to guarantee the appropriate cemented backfilling performance. The functionality of CBM is a powerful tool that can promote the development of cemented backfilling technology. Currently, many scholars all over the world have conducted a great deal of research on cemented backfilling technology. Thus, Fall et al. [1] examined the effect of the curing temperature on the compressive strength of CBM and observed the related micro-structural changes. Ouattara et al. [2] focused on the effects of consistency and unconfined compressive strength of cemented backfilling bodies after the addition of super plasticizers. Aldhafeeri et al. [3] investigated the effects of the curing period and damage on the inner chemical reaction of the cemented backfilling bodies. Tekin et al. [4] established the relation between

the propagation speeds of the cemented backfilling bodies at different curing ages and intensity. Wu et al. [5] determined the optimal proportion and formation mechanism of condensation swelling backfilling composite materials. Deng et al. [6] embedded stress and strain gauges/monitors into the cemented backfilling bodies and derived the stress variation patterns in the backfilling bodies, as well as examining the displacement behavior of roofs supported by the backfilling bodies. Qi et al. [7] measured the resistivity characteristics of the backfilling bodies and proposed the resistivity-based evaluation method of paste backfilling performance. Scholars have achieved numerous promising results in the CBM stress measurements and monitoring but mostly neglected the issues of their functionality [8]. CBM in mines are similar to concretes in main components, and therefore, the relevant studies regarding concretes can provide important clues for the present study. Chuang [9] found that the permeation of conductive fillers into cement substrate can form the conductive network and electron migration channels in the materials, and thus make them self-perceptive of the inner stresses and strains. Pye et al. [10] used carbon ions as the conductive medium and experimentally proved that, after the addition of carbon ions, the volume resistivity of the substrate could drop to the level of conductors. Kang et al. [11] found that the concretes reinforced with carbon fibers can be used for environmental temperature regulation, electrostatic elimination, and antioxidation under ordinary conditions. Naik et al. [12] used high-carbon fly ashes as the conductive medium to replace some types of cement and to prepare conductive cement-based materials with a good workability. Zhao et al. [13] studied the combined capacity of a newly developed slag-blended cement and fly ash as a sustainable solution to improve the mechanical performance of the cemented paste backfill (CPB) system of a copper-gold underground mine. Zhang et al. [14] presented the fluidity and strength evolution of CPB containing the different dosages of polynaphthalene sulfonate, and the physicochemical mechanism of the polynaphthalene sulfonate on the fluidity and strength evolution of CPB was investigated.

Conclusively, previous studies were mainly focused on the transportation and mechanical performances of CBM with the aim of bearing overlying rocks and alleviating the ground depression. Scholars mostly placed the monitoring devices underground, which made their effective recovery and repair impossible, thereby leading to high monitoring cost and poor reliability. Besides, since mine CBM differ significantly from concretes concerning material components, proportions, and structural design, the related research results regarding the functionality of concretes cannot be extended for CBM. Instead, one has to determine the types and shares of the conductive phase in CBM mixtures and, thus, systematically investigate the functionalities of CBM, insofar as these materials possess not only specific structural and mechanical properties but also the perceptivity of backfilling performance and the stress level. The development, application, and exploration of Functional Cemented Backfilling Materials (FCBM) can further revolutionize backfilling mining techniques and generate synergistic effects on safe, high-efficiency, and green mine production.

## 2. Experimental

### 2.1. Test Procedures

Graphite (as the conductive phase) and raw materials (cement, fly ash, and gangue) were weighed, mixed, and stirred. Water was added to the mixture. Afterward, the slurries were poured into the mold for molding, in which the electrodes were buried. After the solidification, the mold was removed, and the molded specimens were placed into the curing box for 7 days of curing. Next, the electrodes were connected to specimens that were subjected to zero and non-zero stress tests (Figure 1). The axial loading system employed the WAW-1000D electro-hydraulic servo testing machine (Xin Te Testing Machine Limited Company of Chang Chun City, Chang Chun, China) [15,16], as shown in Figure 2. Table 1 lists the main chemical ingredients of fly ash and gangue. It can be seen that the main ingredients of fly ash are  $\text{SiO}_2$  and  $\text{Al}_2\text{O}_3$ , which together determine the activity of fly ash. The main ingredients of gangue are  $\text{SiO}_2$  and  $\text{Al}_2\text{O}_3$ , and  $\text{SiO}_2$  is the main aggregate ingredient of FCBM, which determines the strength of FCBM under certain conditions.

Table 1. Chemical ingredients.

Materials	Na <sub>2</sub> O	MgO	Al <sub>2</sub> O <sub>3</sub>	SiO <sub>2</sub>	K <sub>2</sub> O	CaO	Fe <sub>2</sub> O <sub>3</sub>	Other Ingredients
Gangue	0.53	1.8	21.2	54.3	2.2	1.2	5.9	12.87
Fly ash	1.85	2.31	18.5	50.8	1.82	9.6	3.62	11.5

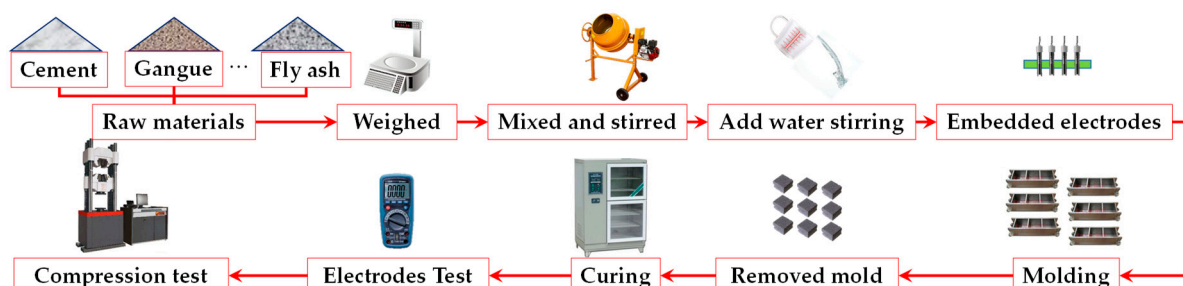


Figure 1. Specimen preparation flow chart.

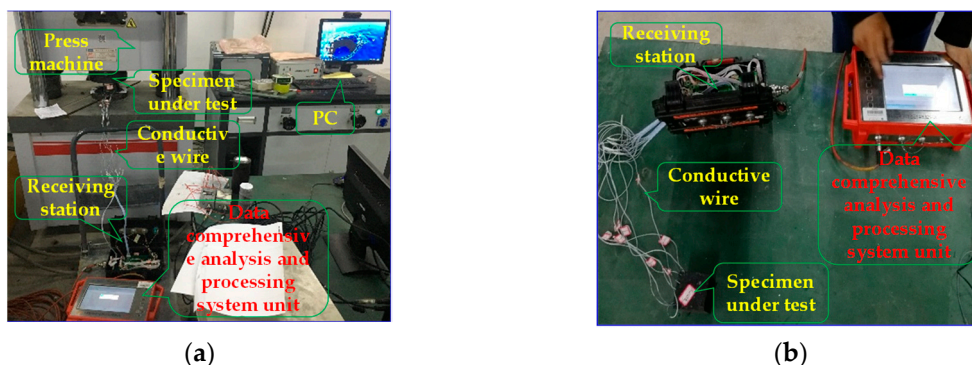


Figure 2. Illustration of resistivity test. (a) non-zero stress conditions. (b) zero stress conditions.

Table 2 lists the proportions of FCBM, in which graphite served as the conductive phase, and the content equaled to the ratio of graphite mass to the total mass of cement, fly ash, gangue, and water-reducing agent.

Table 2. Weights of various ingredients in the prepared specimens (in g).

Specimen No.	Content of Graphite, %	Cement, g	Fly Ash, g	Gangue, g	Water-Reducing Agent, g
1	0	450	760	1360	10
2	5	450	760	1360	10
3	10	450	760	1360	10
4	15	450	760	1360	10
5	20	450	760	1360	10
6	25	450	760	1360	10

According to the particle size test, the gangue particle size was within the range of 0–20 mm, which meets the requirements of cementing backfilling for aggregate particle size. The median particle size (50%) of gangue was 7.16 mm, and the cumulative through particle size of 80% was 9.98 mm. The fly ash particle size was within the range of 0–440 μm, and the fly ash particle size was mainly concentrated in the range of 0–44 μm (61.03%). The particle size distribution is shown in Figure 3.

The embedded copper electrodes were used. In particular, No. 1#~No. 4# electrodes were placed in a row and separated from each other by insulating materials at an interval of 100 mm, while No. 5#~No. 8# electrodes were fixed in the same way. As shown in Figure 4, two arrays of electrodes were arranged in the mold in a parallel way, and the specimens were subjected to pressure in the

direction perpendicular to the test surface. It can be easily observed from the crushed specimens that the true positions of electrodes in the specimens deviated slightly from the designed positions.

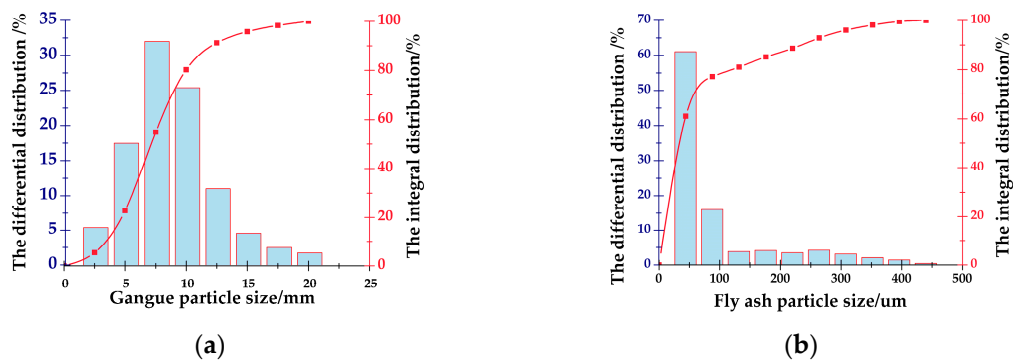


Figure 3. Particle size distribution. (a) Gangue particle size. (b) Fly ash particle size.

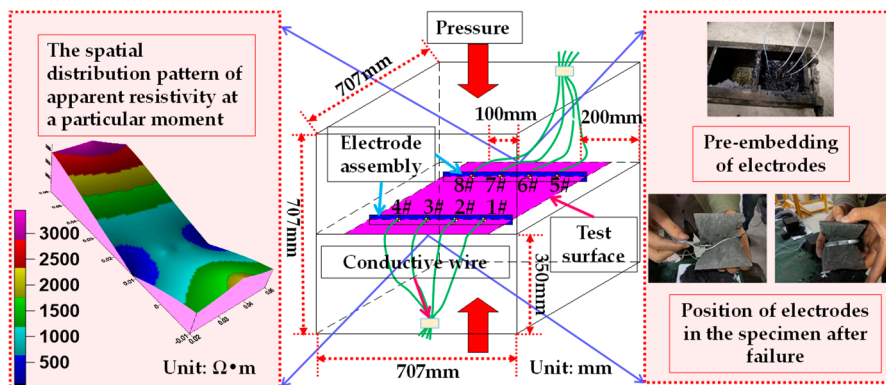


Figure 4. Arrangement of electrodes in specimens.

### 2.2. Principle of Resistivity Measurement

In this experiment, the traditional two- and four-electrode schemes were abandoned [17–22], and the single point power field method (AM method in Figure 5 [23]) was used to measure the resistivity. Two electronic switches were arranged on each electrode. One switch was connected to the array electrode. Power supply gear and measurement gear (the default state, i.e., M-electrode) were set. The switch was connected to the power supply gear (i.e., A-electrode) only after receiving the power supply signal. The other switch was set as the A gear and connected to the power supply.

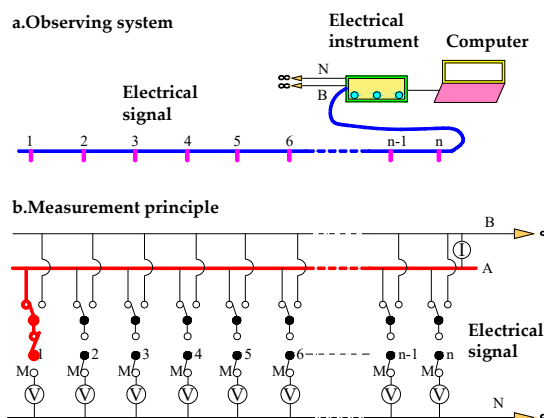


Figure 5. The principle of single-point power supply field measurement.

At the beginning of data acquisition via the AM method, if an electrode receives a power supply signal, the electrode is connected to the power supply gear via the electronic switch, which is also the power supply electrode A (i.e., 1# electrode), while all other electrode switches shift towards the measurement gear (i.e., M-electrode) and are connected to N-electrode via network nodes. During the power supply process of the A-electrode, all M-electrodes simultaneously measure the potential differences with N-electrode (denoted as  $U_{ij}$ , where  $i$  and  $j$  are serial numbers of power-supply electrode and the measurement electrode, respectively) at the preset sampling intervals. The value of  $U_{ij}$  is divided into three parts, namely, before, during and after power supply, corresponding to the natural potential, primary field potential and secondary field potential values. In this way,  $n$  electrodes of the array electrode are sequentially supplied with power, and the remaining electrodes measure the potential, thereby completing the AM method data acquisition of the entire line.

### 2.3. Conductive and Perceptual Mechanism

Insofar as CBM are composite materials, their electrical conductivity is related to conductive mechanisms of composite materials. The latter mechanisms are usually attributed to the percolation effect, tunneling effect in quantum mechanics, and field emission effect in quantum mechanics [24–30], respectively.

Figure 6 [31] illustrates the percolation theory in detail. The electrical conductivity of the material is discontinuous in the range of a certain concentration of conductive filler, and the resistivity of the material will mutate at a certain temperature, which indicates that the dispersion of conductive particles in the polymer matrix has a sudden change at this time. When the concentration of the conductive phase reaches the percolation threshold, conductive paths are formed. Then, electrodes move along the conductive paths, and the material turns from a high insulator into a conductor.

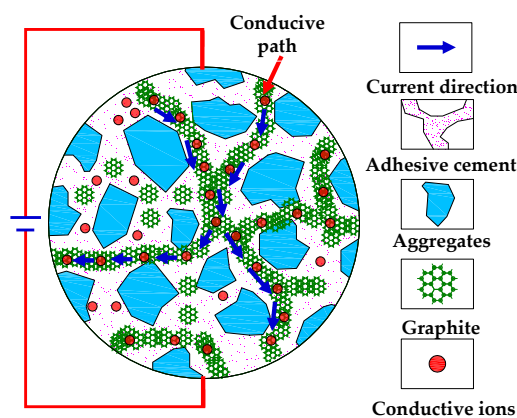


Figure 6. Conductive paths formed by graphite.

Similarly, the perceptual characteristics of FCBM can be explained by perceptual mechanisms of composite materials. These involve the concentration of conductive carriers (including ions, electrons, and holes) [32]. However, the quantity of electric charge of carriers in the material ( $q$ ) is fixed, and therefore, the concentration of carriers changes under the application of stress. According to statistical thermodynamics [33], the number of particles with the energy of  $E_i$  ( $N_{E_i}$ ) is proportional to  $e^{-[E_i/(KT)]}$ , and the concentration of carriers with the power exceeding the barrier energy ( $E_g$ ), denoted as  $n_c$ , can be written as

$$n_c = \frac{1}{N_a} \sum_{E_g}^{\infty} N_{E_i} = \frac{1}{N_a} \int_{E_g}^{\infty} C' e^{-\frac{E_i}{KT}} dE_i = \frac{C'KT}{N_a} e^{-\frac{E_g}{KT}} = CTe^{-\frac{E_g}{KT}} \quad (1)$$

where  $C = C'K/N_a$ .  $C'$  indicates the material constant,  $K$  is the Boltzmann constant, and  $T$  is the absolute temperature (on the Kelvin scale). Accordingly, the concentration of carriers ( $n_c$ ) is related to the values of  $E_g$  and  $T$ . When the materials are deformed under pressure at a constant temperature,

the insulating interval is changed, leading to a shift in barrier energy  $E_g$ . Thus, the  $n_c$  of the material under zero ( $\sigma = 0$ ), and non-zero ( $\sigma \neq 0$ ) stress can be calculated as

$$\begin{cases} n_{z0} = CTe^{-\frac{E_{g0}}{kT}} & \sigma = 0 \\ n_z = CTe^{-\frac{E_g}{kT}} & \sigma \neq 0 \end{cases} \quad (2)$$

The ratio of non-zero and zero stress values from Equation (2) can be derived as follows:

$$\frac{n_z}{n_{z0}} = \frac{CTe^{-\frac{E_g}{kT}}}{CTe^{-\frac{E_{g0}}{kT}}} = e^{\left(\frac{E_{g0}}{kT} - \frac{E_g}{kT}\right)} \quad (3)$$

According to the barrier energy formula, the following expression can be obtained:

$$\begin{cases} E_{g0} = E'_g - \frac{4E'_{g0}}{d_0^2} S & \sigma = 0 \\ E_g = E'_g - \frac{4E'_g}{d^2} S & \sigma \neq 0 \end{cases} \quad (4)$$

where  $S$  denotes the interval barrier area. If the specimen is subjected to stress  $\sigma$ , the respective strain  $\varepsilon$  is generated.  $E'$  is the barrier height, and the material thickness after deformation can be calculated as  $d = d_0 + \Delta d = (1 + \varepsilon)d_0$ , where  $d_0$  is the original thickness of the specimen, and  $\Delta d$  denotes the thickness variation the specimen along the loading direction. Equation (4) can be reduced to the following form:

$$E_g - E_{g0} = \frac{4SE'_{g0}}{d_0^2} \left[ 1 - \frac{1}{(1 + \varepsilon)^2} \right] \quad (5)$$

By substituting Equation (5) into Equation (3), the following expression can be acquired:

$$\frac{n_z}{n_{z0}} = e^{\left\{ \frac{4SE'_{g0}}{kTd_0^2} \left[ \frac{1}{(1+\varepsilon)^2} - 1 \right] \right\}} = e^{\frac{4S\zeta E'_{g0}}{kTd_0^2}} \quad (6)$$

where  $\zeta = [1/(1 + \varepsilon)^2 - 1]$ . According to Equation (6), when the material is under pressure (i.e., subjected to compressive stress), the strain  $\varepsilon$  is negative. With an increase in stress,  $\varepsilon$  is always negative, and the absolute value increases. In other words, when  $\zeta > 0$ ,  $n_z > n_{z0}$ , the concentration of conductive carriers increases, and the material electrical resistance drops. As shown in Figure 7, the material resistance decreases gradually with pressure/stress.

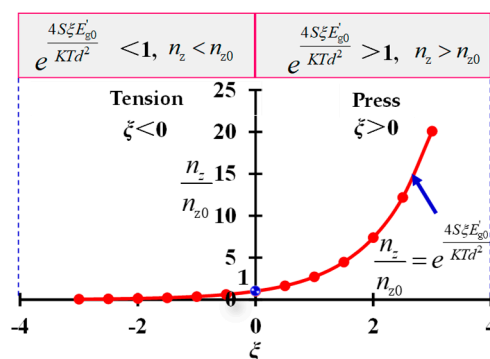
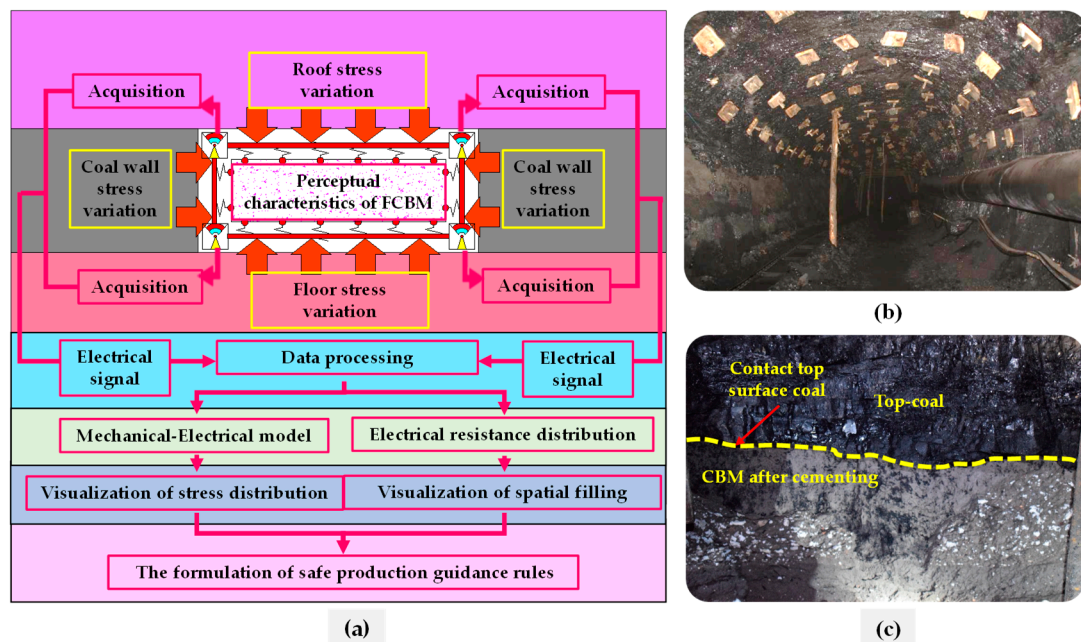


Figure 7. Variation of the concentration of carriers.

When the backfilling materials are filled to the goaf (Figure 8), their electrical signals are acquired via the electric method. Accordingly, on the one hand, the backfilling performance distribution in the goaf can be derived based on their resistivity spatial distribution pattern to determine the

position with a low backfilling ratio. On the other hand, with variation in the stress imposed by external surrounding rocks, the electric signal exhibits varying responses. According to the mechanical–electrical perceptual model, the stress variation rules for the materials pressed by outer surrounding rocks can be obtained. Then, the spatial distribution of backfilling performance and stress field distribution of the surrounding rocks can be assessed, plotted, and visualized. Finally, the spatial distribution of the backfilling performance in the goaf, the stress distribution rules in the surrounding rocks, the high-stress distribution range, surrounding rock damage, as well as inner stress variation in the backfilling materials can be revealed to provide safe production guidance.



**Figure 8.** Illustration of specific application design of cemented backfilling. (a) Design flow of Functional Cemented Backfilling Materials (FCBM) (b) Tunnel segment to be filled by CBM or FCBM (c) Contact between CBM and tunnel rocks.

### 3. Results and Discussion

#### 3.1. Effects of Graphite Content on Mechanical Properties of FCBM

Firstly, uniaxial compressive tests were performed on the specimens with different amounts of the conductive phases to obtain the influence curve of the conductive phase (graphite) content on the mechanical properties of materials, as shown in Figure 9.

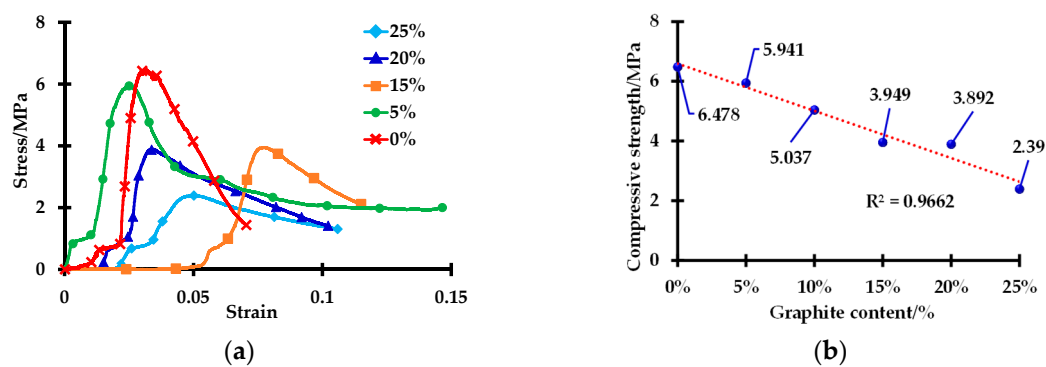


**Figure 9.** Effect of graphite content on the compressive strength of specimens. (a) Stress–strain; (b) relationship curve between strength and graphite content.

According to the stress–strain curves, the FCBM underwent elastic, plastic, and failure stages, whereas the compressive strength sharply dropped with an increase in graphite content. As the graphite content reached 25%, the compressive strength reduced by 63.11%. The compressive test results revealed that the graphite content significantly affected the strength of CBM. The materials with larger contents of graphite exhibited lower compressive strength. This phenomenon can be attributed to the fact that graphite has a low hardness, and different layers in its lattice are piled and bonded via van der Waals forces, with a low friction coefficient and excellent lubricating properties [34–37]. The reduction in the frictional resistance of graphite particles can reduce the adhesive force between aggregates and cementing materials, thereby resulting in a sharply deteriorating strength of the molded specimen.

### 3.2. Effect of Graphite Content on the Apparent Resistivity of FCBM

The addition of graphite imposes an adverse effect on the strength of FCBM but has a positive impact on the apparent resistivity, according to the patterns depicted in Figure 10.

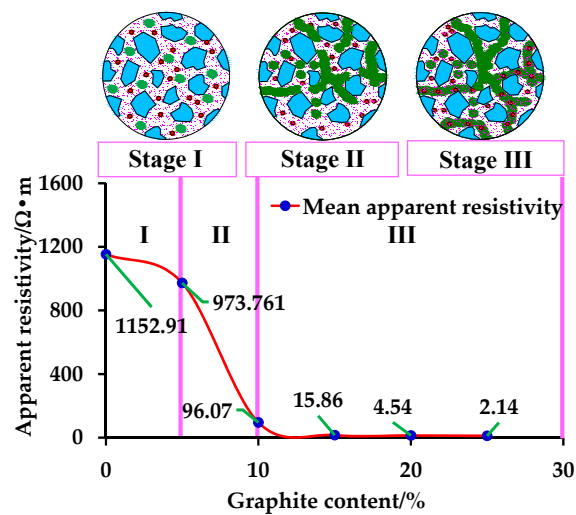


**Figure 10.** Unstressed material internal structure and apparent resistivity versus graphite content.

Figure 10 displays the distribution of apparent resistivity in the CBM with different graphite contents under zero stress conditions, where the curve corresponds to the mean apparent resistivity. As stated above, the apparent resistivity was measured by the network parallel electrical meter. It can be observed that, as the graphite content increases gradually, the apparent resistivity first exhibits a gradual decrease, then sharply drops, and finally reaches the state which fits well with the percolation theory predictions. At a low content of a conductive phase, the material exhibits a high resistivity; as the content of conductive phase increases, a gradual coalescence of inner conductive paths occurs, and initially high resistivity drops to a low level. According to the classical percolation formula (Equation (7)) [38], the fitted percolation threshold of the functional cemented filling material at this proportion is 9.85%, as shown in Figure 11.

$$\rho = \rho_0(m - m_c)^t \quad (7)$$

where,  $\rho$  represents the conductivity of the conductive composite material,  $\rho_0$  is related to the material itself,  $m$  represents the mass fraction of the filler,  $m_c$  represents the percolation threshold, and  $t$  represents the critical index related to the structure of the conductive network.

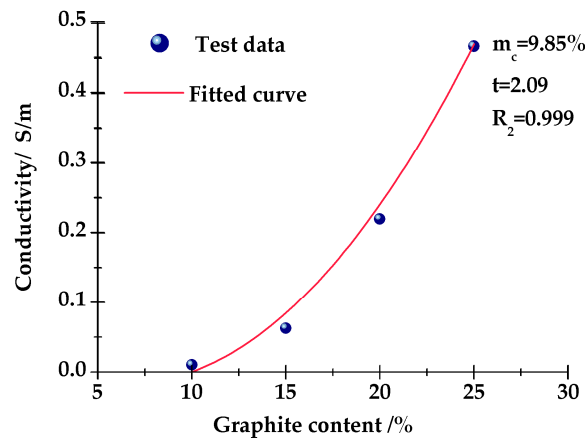


Figure 11. Percolation test data and best-fitting curve.

### 3.3. Spatial Distribution Rules of Apparent Resistivity in FCBM

Using a network parallel electrical meter, the apparent resistivity values of tested specimens with different graphite contents were measured. The spatial distributions of the apparent resistivity in specimens before and after failure (i.e., before and after the stress generation) are shown in Figure 12a,b, respectively.

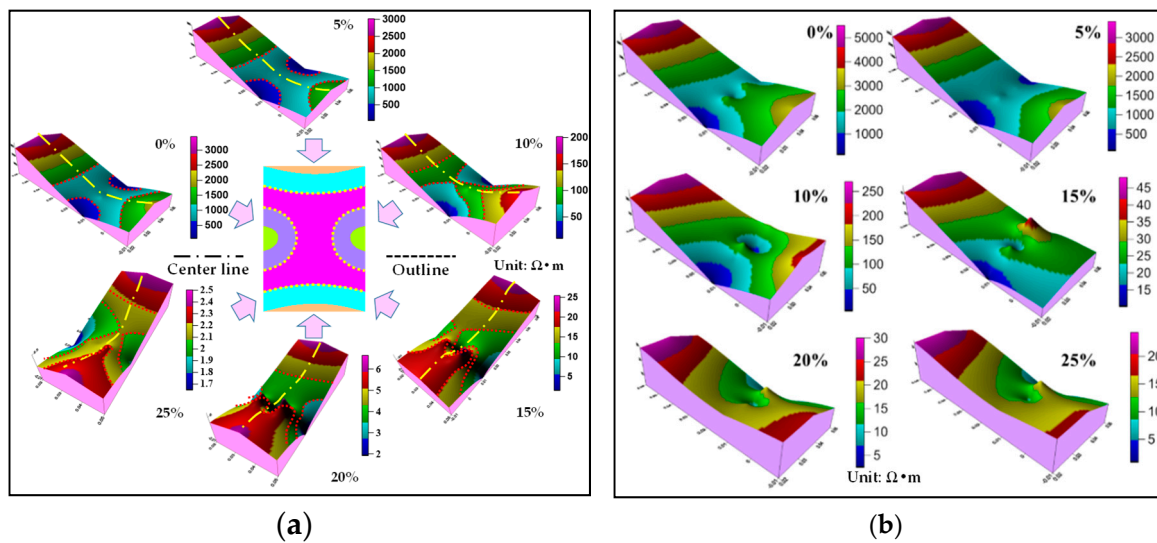


Figure 12. Spatial distributions of apparent resistivity in specimens before failure and after failure. (a) Before failure. (b) After failure.

As shown in Figure 12a, the apparent resistivity of materials under study can be adequately measured by the network parallel electric meter. Before the specimen failure, the apparent resistivity in the materials with different contents of the conductive phase exhibit similar X-shaped radial distribution patterns. In particular, the minimum apparent resistivity is observed in the center of materials and increases gradually with the distance from the center. Moreover, the variation rate along the center line is the most consistent. Besides, as the content of the conductive phase increases gradually, the X-shaped radial distribution pattern of apparent resistivity in the material becomes more irregular. This can be explained as follows: with a gradual decrease in the apparent resistivity, its relative difference in the material drops, and the spatial distribution variation of the apparent resistivity becomes more distinct. Additionally, as shown in Figure 12b, the apparent resistivity after failure exhibits different distribution rules in the material, which control its further spatial distribution evolution. The development of fractures in the material imposes a very strong effect on the spatial

distribution of the apparent resistivity. Therefore, in actual engineering, the spatial distribution rules of apparent resistivity can be used as criteria for judging whether the material is damaged or not.

### 3.4. Variation of Apparent Resistivity of FCBM at Different Deformation Stages

Next, the variation rules of apparent resistivity in specimens with graphite contents of 0% and 15% at different deformation stages were investigated. The results obtained are shown in Figure 13. As the strain increases gradually, the apparent resistivity first remains unchanged and then increases slowly. To be specific, at the elastic phase (OA-segment of Stage I), the spatial distribution of the apparent resistivity exhibits no changes, i.e., no fracture sites are developed in the specimen at this stage, while its resistance exhibits a slight change. At the plastic stage (AB-segment of Stage II), the spatial distribution of apparent resistivity changes slightly, while fractures start to develop in the specimen, and its resistance starts to change. At the failure stage (BC-segment of Stage III), the spatial distribution of apparent resistivity exhibits a strong response with an increase in stress. During this stage, fractures are well-developed, and resistance changes significantly. Before the failure, the mechanical–electrical response does not change; fractures develop gradually in the specimen after the failure; and the apparent resistivity starts to increase. Accordingly, this response exhibits no perceptual characteristics, i.e., CBMs with no addition of graphite possess no perceptual characteristics.

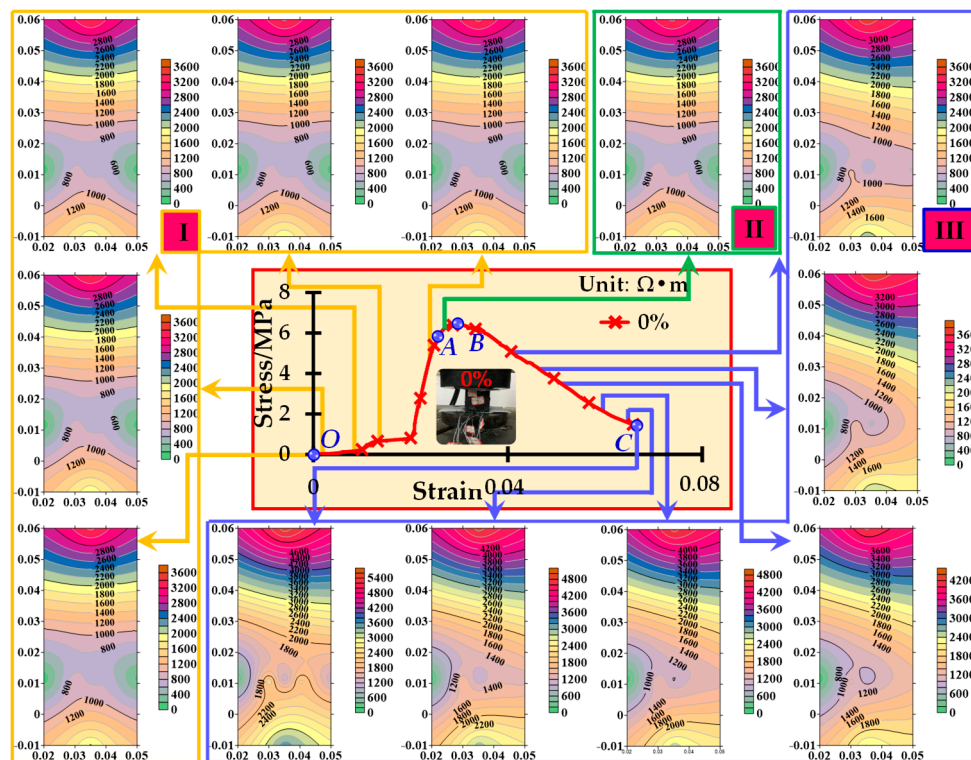


Figure 13. Variation charts of specimen with no graphite addition at different stages.

Figure 14 displays the spatial distribution variation of the stress–strain curve and apparent resistivity of the specimen with 15% graphite at different stages. As the strain gradually increases, the apparent resistivity first drops and then increases. At the elastic stage, the apparent resistivity drops slowly with an increase in stress/strain. At the plastic phase, insufficient data were acquired for such a short period; however, in contrast with the conditions at the elastic step, the apparent resistivity still drops with the strain/stress increase. It should be noted that the specimen is slightly damaged at this stage, i.e., perceptual characteristics still exist within a certain damage range. Finally, at the failure stage, the apparent resistivity increases with strain, whereas the material becomes damaged, the fractures propagate gradually, and the apparent resistivity also increases steadily.

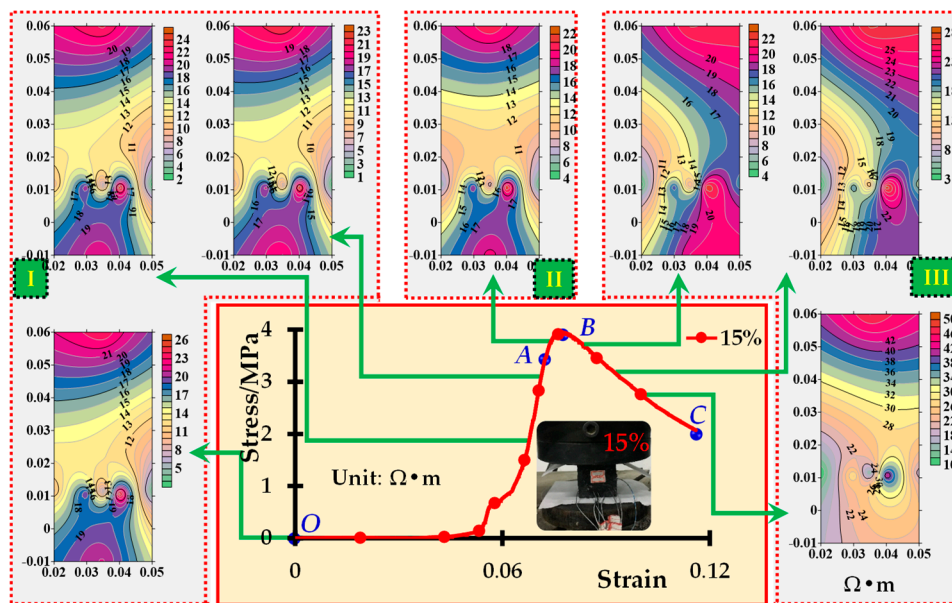


Figure 14. Variation charts of the specimen with 15% graphite at different stages.

Through the comparative analysis, it can be concluded that conventional CBMs used in coal mines have no perceptual characteristics but acquire them after the addition of a certain amount of conductive phase. This implies that the addition of graphite can modify traditional CBMs into FCBMs. As shown in Figures 13 and 14, the spatial distribution of the apparent resistivity in FCBM exhibits different variation rules at various stages. At the elastic and plastic stages, the apparent resistivity drops gradually with strain/stress. In contrast, at the failure stage, the apparent resistivity of the backfilling material increases gradually with strain.

### 3.5. Further Analysis of the Variation of Apparent Resistivity of FCBM

In practical production, due to the effect of mining, the stress field in the surrounding rock is not stationary. It is necessary to investigate the effects of repetitive loading on the apparent resistivity of FCBM. Meanwhile, to validate the reversibility of perceptual characteristics at the elastic stage, one-third of the full load was first applied to the specimen with 20% graphite. After unloading, it was subjected to the full load. Figure 15 displays the variation cloud charts of the apparent resistivity in the above loading process.

During the application of the one-third load level (corresponding to the elastic stage), the apparent resistivity of the specimen drops with strain. After unloading, the apparent resistivity can be recovered to the initial value, which also exhibits same variation rules with the subsequent full-loading process. Accordingly, it can be concluded that the perceptual characteristics of FCBM are reversible at this stage. In other words, as the applied stress is gradually reduced to zero, the initial zero-stress value of the specimen's apparent resistivity can be progressively recovered. At the plastic stage, certain damage occurs in the materials; however, the materials still possess specific perceptual characteristics, since the damage is slight. Unfortunately, the material damage at this stage is unrecoverable, which leads to irreversible changes in the material perceptual properties at this stage. This implies that the initial state of the apparent resistivity cannot be recovered after unloading. At the failure stage, numerous fractures/cracks develop in the material, its structure becomes damaged, and its initial state cannot be recovered, i.e., the material no longer possesses perceptual characteristics. Overall, due to the reduction of elastic modulus at the plastic and damage stages, unrecoverable damage appears in the material, which can account for irreversible changes in the perceptual characteristics of FCBM at these two stages. Conclusively, FCBM exhibit reversible perceptual characteristics only at the elastic stage.

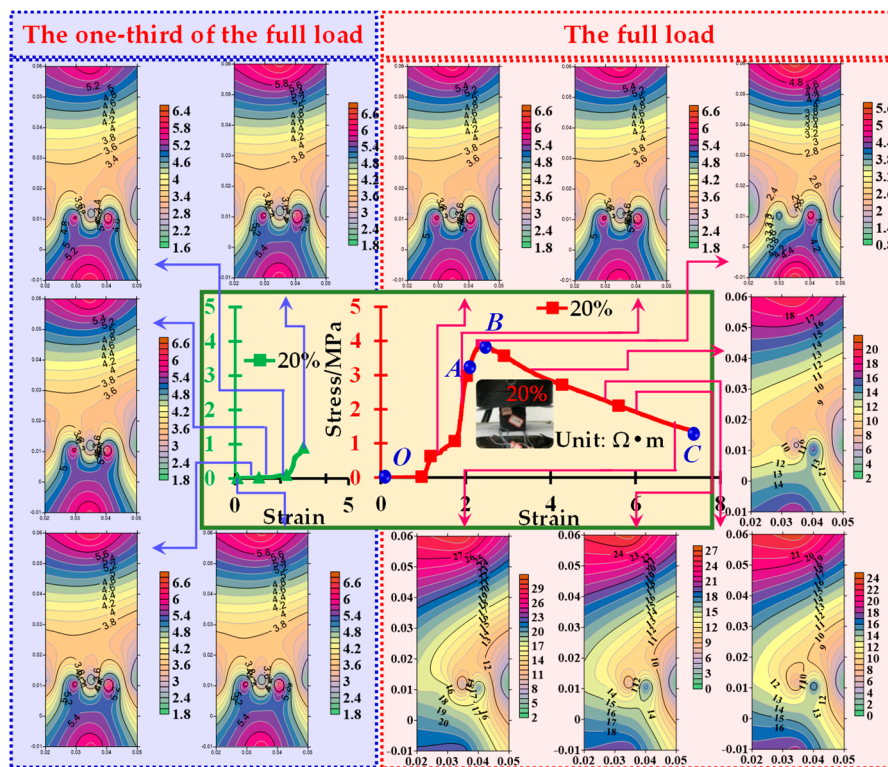


**Figure 15.** Variation cloud charts of the specimen with 20% graphite at different stages in the cyclic loading process.

According to the variation rules of the apparent resistivity of FCBM with different graphite contents under different loads, the following guidelines for practical engineering can be formulated:

- (1) The spatial distribution characteristics of the apparent resistivity can be used for judging whether the material is subjected to loading or undergoes a failure.
- (2) The spatial distribution of electrical properties can be used for reflecting spatial backfilling performances in the goaf.
- (3) The recoverability of the apparent resistivity original state can be used for judging whether the material undergoes the elastic or plastic stage.
- (4) The stress field distribution in the surrounding rock can be derived based on the proposed mechanical–electrical perceptual model.

In terms of the perceptual mechanism described in Section 2.3, the results are well verified. With the progress of the experiment, the material strain value negatively increases, that is, if  $\xi > 0$ , then  $n_z/n_{z0} > 1$ . Consequently, the concentration of conducting carriers is larger than the original concentration, leading to resistance reduction. However, the material no longer has the perceptual characteristics when damaged, so the perceptual mechanism is not applicable. In conclusion, the concentration of conductive carriers can well explain the perceptual characteristics of materials.

#### 4. Conclusions

Based on previous findings, this study selected graphite as the conductive phase for exploring the possibility of modifying traditional CBM into functional ones (FCBM). Besides, the electrical sensing method was adopted for the first time in the geophysical field to assess the spatial distribution patterns of material resistivity, in order to overcome the deficiency of traditional two- or four-electrode schemes that fail to derive the spatial resistivity distribution characteristics in the specimen. Furthermore, the spatial distribution rules of the apparent resistivity of FCBM with different graphite contents under no stress and the related variation rules under mechanical–electrical coupled action were revealed,

which can provide a theoretical basis for further investigations of FCBM. The following conclusions may be drawn:

(1) Using the electrical method, spatial apparent resistivity values of Functional Cemented Backfilling Materials (FCBM) with different contents of graphite before and after loading (i.e., with zero and non-zero stress values) were measured. The application design method of FCBM was also elaborated for the formulation of judgment criteria in engineering applications. The present study can inspire a new direction in smart-controlled underground mining.

(2) The addition of graphite can significantly reduce the structural, mechanical properties of FCBM, whose compressive strength drops as the graphite content increases. However, the addition of graphite imposes a positive effect on the apparent resistivity of the material. Moreover, it was experimentally validated that FCBMs in mines exhibit the percolation effect, and the percolation threshold is 9.85%.

(3) The apparent resistivity of cemented backfilling material exhibits an X-shaped radial distribution pattern at both the elastic and plastic stages. The apparent resistivity at the center of the specimen is the smallest and gradually increases with a distance from the center; furthermore, the apparent resistivity drops most rapidly along the center line. At the failure stage, the apparent resistivity exhibits different distribution rules in specimens with various contents of graphite. These distribution rules are mainly controlled by the development of fractures in FCBM specimens.

(4) Traditional CBMs in mines possess no perceptual characteristics; however, as the content of the conductive phase exceeds the percolation threshold, these materials exhibit a perceptual characteristic. The CBM apparent resistivity is negatively correlated with the stress/strain at the elastic and plastic stages, while it exhibits a positive correlation with stress/strain at the failure stage. The CBM specimens show no functionality after failure, insofar as their perceptual characteristics are reversible only at the elastic stage.

**Author Contributions:** All the authors contributed to this paper. H.L. prepared and edited the manuscript. J.Z. provided theoretical and methodological guidance in the research process. W.Z. partially participated in the literature search. F.G. processed the data in this article. H.Y. and T.A. participated in revising the manuscript.

**Funding:** This research was funded by the National Key R&D Program of China [grant number 2018YFC0604704] and National Science Fund for Distinguished Young Scholars [grant number 51725403].

**Acknowledgments:** We are grateful to China University of Mining and Technology for providing us with the experimental platform and all the reviewers for their specific comments and suggestions.

**Conflicts of Interest:** The authors declare no conflict of interest.

## References

1. Fall, M.; Célestin, J.C.; Pokharel, M.; Touré, M. A contribution to understanding the effects of curing temperature on the mechanical properties of mine cemented tailings backfill. *Eng. Geol.* **2010**, *114*, 397–413. [[CrossRef](#)]
2. Ouattara, D.; Belem, T.; Mbonimpa, M.; Yahia, A. Effect of superplasticizers on the consistency and unconfined compressive strength of cemented paste backfills. *Constr. Build. Mater.* **2018**, *181*, 59–72. [[CrossRef](#)]
3. Aldhafeeri, Z.; Fall, M. Time and damage induced changes in the chemical reactivity of cemented paste backfill. *J. Environ. Chem. Eng.* **2016**, *4*, 4038–4049. [[CrossRef](#)]
4. Tekin, Y.; Ercikdi, B.; Karaman, K.; Külekçi, G. Assessment of strength properties of cemented paste backfill by ultrasonic pulse velocity test. *Ultrasonics* **2014**, *54*, 1386–1394.
5. Lan, W.T.; Wu, A.X. Formulation optimization and formation mechanism of condensate expansion and filling composites. *Acta Mater. Compos. Sin.* **2019**, online first.
6. Deng, X.J. *Ground Control Mechanism of Mining Extra-thick Coal Seam Using Upward Slicing Longwall-Roadway Cemented Backfilling Technology*; China University of Mining and Technology: Xuzhou, China, 2017.
7. Qi, T.Y.; Feng, G.R.; Zhang, X.J.; Yu, C.T.; Liu, H.F.; Kang, L.X. The application of resistivity evaluating filling effect method in Xinyang coal mine. *J. Min. Saf. Eng.* **2017**, *34*, 302–309.

8. Liu, L.; Xin, J.; Zhang, B.; Zhang, X.Y.; Wang, M.; Qiu, H.F.; Chen, L. Basic Theories and Applied Exploration of Functional Backfill in Mines. *J. China Coal Soc.* **2018**, *43*, 1811–1820.
9. Chung, D.D.L. Structural health monitoring by electrical resistance measurement. *Smart Mater. Struct.* **2001**, *10*, 624. [[CrossRef](#)]
10. Pye, G.B.; Myers, R.E.; Arnott, M.R. Conductive concrete compositions containing carbonaceous particles. *Chem. Abstr.* **2001**, *58*, 76.
11. Kang, S.H.; Ko, J.S.; Kim, J.J. Conductive carbon fiber composite for Concrete Structures. *Chem. Ab-stracts.* **2001**, *57*, 58.
12. Tarun, R.N.; Rudolph, N.K.; Ramme, B.W.; Chun, Y.M.; Kumar, R. High-carbon fly ash in manufacturing conductive CLSM and concrete. *J. Mater. Civil. Eng.* **2006**, *18*, 743–746.
13. Zhao, Y.; Soltani, A.; Taheri, A.; Karakus, M.; Deng, A. Application of Slag–Cement and Fly Ash for Strength Development in Cemented Paste Backfills. *Minerals* **2019**, *9*, 22. [[CrossRef](#)]
14. Zhang, J.; Deng, H.W.; Taheri, A.; Deng, J.R.; Ke, B. Effects of Superplasticizer on the Hydration, Consistency, and Strength Development of Cemented Paste Backfill. *Minerals* **2018**, *8*, 381. [[CrossRef](#)]
15. Yan, H.; Zhang, J.X.; Wang, J.Q.; Zhou, N.; Zhang, S. Multi-fractal characteristics of particle size distribution of granular backfilling materials under different loads. *Mater. Test.* **2018**, *60*, 202–208. [[CrossRef](#)]
16. Li, M.; Zhang, J.X.; Sun, K.; Zhang, S. Influences of Lateral Loading on Compaction Characteristics of Crushed Waste Rock Used for Backfilling. *Minerals* **2018**, *8*, 552. [[CrossRef](#)]
17. Volkmann, J.; Klitzsch, N. Wideband impedance spectroscopy from 1mHz to 10MHz by combination of four- and two-electrode methods. *J. Appl. Geophys.* **2015**, *114*, 191–201. [[CrossRef](#)]
18. Uvarov, N.F.; Ulihin, A.S.; Bepalko, Yu.N.; Ereemeev, F.; Krasnov, A.V.; Skriabin, P.I.; Sadykov, V.A. Study of Proton Conductivity of Composite Metal-Ceramic Materials Based on Neodimium Tugstates Using a Four-Electrode Technique with Ionic Probes. *Int. J Hydrogen Energy* **2018**, *43*, 21–27. [[CrossRef](#)]
19. Karthick, S.; Velu, S.; Seung, J.K.; Han, S.L.; Rethinam, N.; Dong, J.P. A Novel in-Situ Corrosion Monitoring Electrode for Reinforced Concrete Structures. *Electrochim. Acta* **2018**, *259*, 29–44. [[CrossRef](#)]
20. Lee, B.; Seokhoon, O. Modified Electrical Survey for Effective Leakage Detection at Concrete Hydraulic Facilities. *J. Appl. Geophys.* **2018**, *149*, 14–30. [[CrossRef](#)]
21. Jakubas, A.; Paweł, J. The Influence of Electrode Size on Resistance Measurement in the Modified Four-Electrodes Method. *Measurement* **2017**, *108*, 34–40. [[CrossRef](#)]
22. Mironov, V.S.; Kim, J.K.; Park, M.; Lim, S.; Cho, W.K. Comparison of electrical conductivity data obtained by four-electrode and four-point probe methods for graphite-based polymer composites. *Polym. Test.* **2007**, *26*, 547–555. [[CrossRef](#)]
23. Liu, S.D.; Wu, R.X.; Zhang, P.S.; Cao, Y. Three-dimensional parallel electric surveying and its applications in water disaster exploration in coal mines. *J. China Coal Soc.* **2009**, *34*, 927–932.
24. Tkalya, E.; Ghislandi, M.; Otten, R.; Lotya, M.; Alekseev, A.; Paul, V.D.S. Experimental and theoretical study of the influence of the state of dispersion of graphene on the percolation threshold of conductive graphene/polystyrene nanocomposites. *ACS Appl. Mater. Interface* **2014**, *6*, 15113–15121. [[CrossRef](#)] [[PubMed](#)]
25. Lu, X.; Yvonnet, J.; Detrez, F.; Bai, J. Multiscale modeling of nonlinear electric conductivity in graphene-reinforced nanocomposites taking into account tunnelling effect. *J. Comput. Phys.* **2017**, *337*, 116–131. [[CrossRef](#)]
26. Beek, L.K.H.V.; Pul, B.I.C.F.V. Internal field emission in carbon black-loaded natural rubber vulcanizates. *J. Appl. Polym. Sci.* **2010**, *6*, 651–655. [[CrossRef](#)]
27. Wang, G.; Wang, C.; Zhang, F.; Yu, X. Electrical percolation of nanoparticle-polymer composites. *Comp. Mater. Sci.* **2018**, *150*, 102–106. [[CrossRef](#)]
28. Bo, S.; Dong, L.; Li, M.Q.; Liu, B.; Kyunghoon, K.; Xu, X.F.; Zhou, J.; Liu, J. Thermal Percolation in Composite Materials with Electrically Conductive Fillers. *Appl. Phys. Lett.* **2018**, *113*, 041902.
29. Han, B.Z.; Zhang, L.Y.; Han, B.G.; Liu, L.Y.; Hu, Z.X. Piezoresistive composites based on quantum tunneling effect. *J. Funct. Mater.* **2008**, *39*, 931–934.
30. Gong, J.; Tang, Y.; Yang, P. Investigation on field emission properties of graphdiyne-BN composite. *J. Mol. Struct.* **2014**, *1064*, 32–36. [[CrossRef](#)]
31. Ruschau, G.R.; Yoshikawa, S.; Newnham, R.E. Resistivities of conductive composites. *J. Appl. Phys.* **1992**, *72*, 953–959. [[CrossRef](#)]

32. Wei, J.; Zhao, L.L.; Zhan, Q.; Nie, Z. Development of Seebeck Effect of Carbon Fiber Reinforced Cement-based Composites. *Mater. Rev.* **2017**, *31*, 84–89.
33. Liang, X.X. *Statistical Thermodynamics*; Inner Mongolia University Press: Hohhot, China, 2000.
34. Dong, Y.; Liu, C.; Duan, Z.; Birahima, G.; Tao, Y.; Zhang, Y. Molecular dynamics simulations of stiffness-dependent friction of graphene. *J. Southeast Univ.* **2017**, *47*, 28–32.
35. Kalin, M.; Poljanec, D. Influence of the contact parameters and several graphite materials on the tribological behaviour of graphite/copper two-disc electrical contacts. *Tribol. Int.* **2018**, *126*, 192–205. [[CrossRef](#)]
36. Liu, H.; Li, L. Graphitic materials: Intrinsic hydrophilicity and its implications. *Extrem. Mech. Lett.* **2017**, *14*, 44–50. [[CrossRef](#)]
37. Androulidakis, C.; Koukaras, E.N.; Hadjinicolaou, M.; Galiotis, C. Non-Eulerian behavior of graphitic materials under compression. *Carbon* **2018**, *138*, 227–233. [[CrossRef](#)]
38. Kirkpatrick, S. Percolation and conduction. *Rev. Modern Phys.* **1973**, *45*, 574–588. [[CrossRef](#)]



© 2019 by the authors. Licensee MDPI, Basel, Switzerland. This article is an open access article distributed under the terms and conditions of the Creative Commons Attribution (CC BY) license (<http://creativecommons.org/licenses/by/4.0/>).